Periodic deformation of semiflexible colloidal chains in eccentric time-varying magnetic fields

OPEN ACCESS
IOP Publishing
Journal of Physics: Condensed Matter
J. Phys.: Condens. Matter **34** (2022) 184005 (17pp)
https://doi.org/10.1088/1361-648X/ac533a

Periodic deformation of semiflexible colloidal chains in eccentric time-varying magnetic fields

Aldo Spatafora-Salazar[1], Lucas H P Cunha[1,2] and Sibani Lisa Biswal[1,*]

[1] Department of Chemical and Biomolecular Engineering, Rice University, Houston, TX 77005, United States of America
[2] Center for Theoretical Biological Physics, Rice University, Houston, TX 77030, United States of America

E-mail: biswal@rice.edu

Received 9 November 2021, revised 24 January 2022
Accepted for publication 9 February 2022
Published 1 March 2022

Abstract

Elastic filaments driven out of equilibrium display complex phenomena that involve periodic changes in their shape. Here, the periodic deformation dynamics of semiflexible colloidal chains in an eccentric magnetic field are presented. This field changes both its magnitude and direction with time, leading to novel nonequilibrium chain structures. Deformation into S-, Z-, and 4-mode shapes arises via the propagation and growth of bending waves. Transitions between these morphologies are governed by an interplay among magnetic, viscous, and elastic forces. Furthermore, the periodic behavior leading to these structures is described by four distinct stages of motion that include rotation, arrest, bending, and stretching of the chain. These stages correspond to specific intervals of the eccentric field's period. A scaling analysis that considers the relative ratio of viscous to magnetic torques via a critical frequency illustrates how to maximize the bending energy. These results provide new insights into controlling colloidal assemblies by applying complex magnetic fields.

Keywords: paramagnetic colloids, periodic deformation, semiflexible chains, nonequilibrium, magnetic fields

S Supplementary material for this article is available online

(Some figures may appear in colour only in the online journal)

1. Introduction

Semiflexible filaments undergo periodic configurational dynamics when driven out of equilibrium [1]. This is usually achieved by subjecting the filaments to external flow fields or by the activity of molecular motors. Examples include the buckling-tumbling events and snaking motion of semiflexible polymers in shear flows [2–4], continuous cycles of compression and stretching under oscillatory extensional flows [5], helical coiling and relaxation when passing through successive micro-channels of varying width [6, 7], the undulating bodies of small filamentous organisms [8, 9], and the beating of flagella and cilia that power cell propulsion and other biological processes [10, 11]. The complex dynamics and the variety of shapes attainable by semiflexible filaments have sparked the design of artificial filaments that exhibit novel deformation behaviors when externally driven to nonequilibrium conditions [12–14].

The directed assembly of colloidal particles into chain structures is an effective method to build artificial filaments that act as model systems of polymers and fibers in equilib-

* Author to whom any correspondence should be addressed.

rium [15, 16] and nonequilibrium conditions [17–19]. Such colloidal chains can be tailored with elastic properties by incorporating macromolecular linkers that bond adjacent particles together during the assembly process [12, 20, 21]. Paramagnetic colloids have received significant attention as building blocks of model semiflexible filaments for several reasons. First, under a static magnetic field, the particles acquire dipoles that favor a head-to-tail alignment due to anisotropic interactions, directing the assembly of the particles into linear chains [22, 23]. Second, the induced dipoles respond quickly to changes in the direction of an external magnetic field, facilitating the manipulation of the chains. Finally, the strength of the interparticle dipolar interactions is easily tunable by changing the magnitude of the applied magnetic field [23–25]. This responsive nature, combined with the flexibility of the linkers, allows for unique dynamics of these chain assemblies [26, 27].

Studies of elastic paramagnetic chains driven away from equilibrium by time-varying fields have mainly focused on the effects of circularly rotating magnetic fields [28]. Interaction of the elastic chain with the surrounding fluid while undergoing field-induced rotation in planar circular fields leads to a plethora of rotational and configurational dynamics, depending on the flexibility of the chain and on field parameters like magnitude and frequency. These dynamics include synchronous rotation [29], asynchronous rigid rotation [30], asynchronous rotation with wagging ends [31, 32], coiling from the ends to the center leading to a collapsed rotating structure [31, 33, 34], and folding of the chain into an effectively shorter configuration that can also sustain synchronous rotation [30, 31]. In short, these planar circular fields induce chain rotation and can lead to interesting deformation behaviors, but they are not periodic in most cases. Although the wagging dynamics showcase periodicity, they are also susceptible to perturbations that lead to the collapse of the chain via coiling of one of its ends. Thus, the conventional circular field tends to fold semiflexible chains into small structures that do not display periodic patterns in their deformation.

Applying other types of magnetic fields represents a strategy to achieve periodic shape changes in the chains akin to those observed in flowing or active semiflexible polymers. Recent studies have characterized the chain response under conical fields that alter the shape into novel helical configurations [35, 36]. However, the morphology does not seem to change periodically unless the chains are tethered on one end to a surface [37, 38]. An eccentric field, which is a type of planar field in which both the direction as well as the magnitude vary with time, has been applied to systems of a few unlinked particles leading to periodic changes in interparticle spacing [39]. This observation points at the potential application of eccentric fields to periodically deform paramagnetic chains that are free on both ends. Here, we find that this is indeed the case.

In this paper, we describe the periodic configurational dynamics of DNA-linked paramagnetic chains that arise in eccentric magnetic fields. Depending on the frequency of the eccentric field, the chains bend into three different characteristic morphologies. These configurations are consistent in both experiments and numerical simulations. The morphologies include a conventional S-shape and two novel patterns for chains in time-varying fields: a highly coarsened Z-shape and a four-mode structure. After acquiring these shapes, the chains rapidly stretch back to the linear configuration. We decompose the deformation dynamics of the chains within a single period into four distinct stages of motion: (I) rotation of the chain, (II) arrest of the angular motion, (III) bending and coarsening, and (IV) stretching and realignment of the deformed chain. From this analysis, we are able to explain the dynamics in terms of an interplay among magnetic, viscous, and elastic forces. Key geometric parameters are used to characterize the extent of chain deformation. We find that the peak values in the deformation parameters follow a nonmonotonic trend that scales with the critical magnetoviscous frequency of the chain, allowing us to identify the field parameters that maximize the bending energy during the deformation events. Overall, our results provide new understanding of how semiflexible filaments behave under nonequilibrium conditions.

2. Experimental methods

2.1. Chain assembly

Semiflexible colloidal chains were prepared from streptavidin-coated superparamagnetic particles of diameter $2a = 1$ μm (MyOne Streptavidin C1 Dynabeads, Invitrogen). The particles were diluted to 0.00125% w/v in PBS-azide and mixed with 2000 bp double-stranded DNA labeled with biotin at the 5′ ends [40, 41]. The concentrations of these components in the final solution were 10 mM PBS, 0.01% w/v sodium azide, and 5 nM DNA.

The chains were synthesized within a sample cell consisting of two microscope coverslips spaced by double-sided tape (thickness: 90 μm). The coverslips were cleaned with oxygen plasma at 600 mTorr for 1 min, immersed in a KOH bath for 30 min, rinsed thoroughly with DI water, and then dried with nitrogen. An aliquot of 40 μL of the colloidal suspension was flowed into the cell, which was then sealed with epoxy adhesive (Hardman Double/Bubble). The particles sedimented to the bottom of the cell due to their large density (1.8 g cm^{-3}), ensuring their confinement to a quasi-2D plane. Contact with the bottom coverslip was prevented due to electrostatic repulsion. The cell was placed for 90 min between two permanent magnets that produced a static magnetic field of 11.6 kA m^{-1}. Due to the dipolar and DNA interactions, the superparamagnetic particles align their induced magnetic dipoles by assembling into linear chains of linked particles, as depicted in figure 1(a). This linking procedure was performed on a heat plate at 60 °C to enhance the diffusion of the DNA toward the particle surfaces. The biotinylated DNA links the adjacent streptavidin-coated particles, preventing disassembly when the external field is removed and conferring elasticity to the chain. The average persistence length of the chains was determined to be $l_p = 0.56 \pm 0.17$ mm, using Fourier mode decomposition of the shape fluctuations, along the contour of several chains, caused by thermal motion [16, 24, 31, 40]. Figure 1(b) illustrates these fluctuations in the shape of a chain consisting of 31 particles.

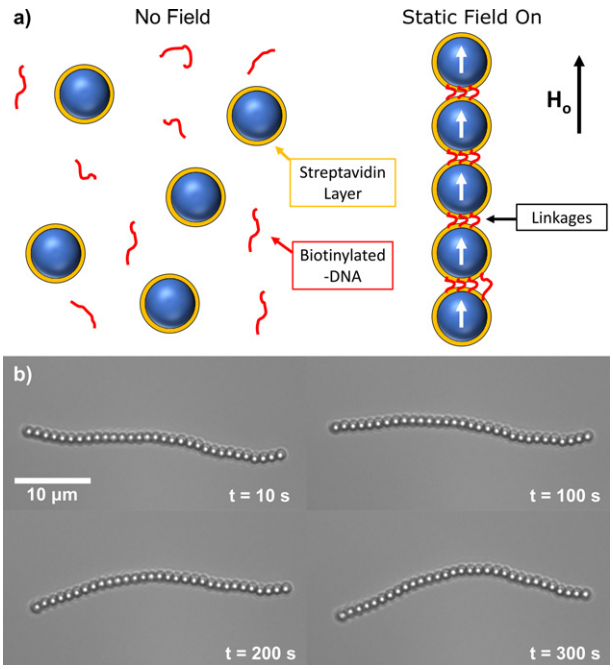

Figure 1. (a) Directed assembly of paramagnetic particles into semiflexible chains under a static magnetic field employing surface chemistry and DNA linkers. Left: schematic of the main components necessary to assemble the chains. In the absence of a magnetic field, the paramagnetic particles are unpolarized. The particles are functionalized with streptavidin and mixed with biotinylated DNA in a buffer solution. Right: schematic of the assembled particles when the field is turned on. The paramagnetic particles acquire magnetic dipoles (white arrows) with the same direction as the external field. Particles assemble into a chain to align the dipoles head-to-tail. The biotin ends of the DNA bind to streptavidin sites on the particles. The DNA acts as a linker that confers elastic properties to the chain. (b) Snapshots of an assembled chain of 31 particles ($2a = 1$ μm) linked by 2000 bp DNA after the field is turned off. The paramagnetic particles do not disassemble despite the loss of their dipoles due to the linkers. Shape fluctuations caused by thermal motion can be observed over time, demonstrating the semiflexible nature of the chains.

2.2. *Eccentric time-varying field*

The eccentric time-varying field consists of two perpendicular sinusoidal waves that have an additional DC offset signal [39]

$$\mathbf{H}_x(t) = H_o\left[\sin(2\pi f t) + \lambda_x\right]\hat{\mathbf{e}}_x \tag{1a}$$

$$\mathbf{H}_y(t) = H_o\left[\cos(2\pi f t) + \lambda_y\right]\hat{\mathbf{e}}_y \tag{1b}$$

where $\mathbf{H}_x(t)$ and $\mathbf{H}_y(t)$ are the time-varying components of the magnetic field, λ_x and λ_y are the DC offset constants, H_o is the amplitude of the field, f is the frequency, and t is time. If $\lambda_x = \lambda_y = 0$, equation (1) reduces to that of a conventional circular field with varying direction but constant magnitude. Hence, $\lambda_x = \lambda_y \neq 0$ is the necessary ingredient to vary both the direction and strength of the magnetic field. Throughout the present work, the DC offsets were set to $\lambda_x = \lambda_y = 1$.

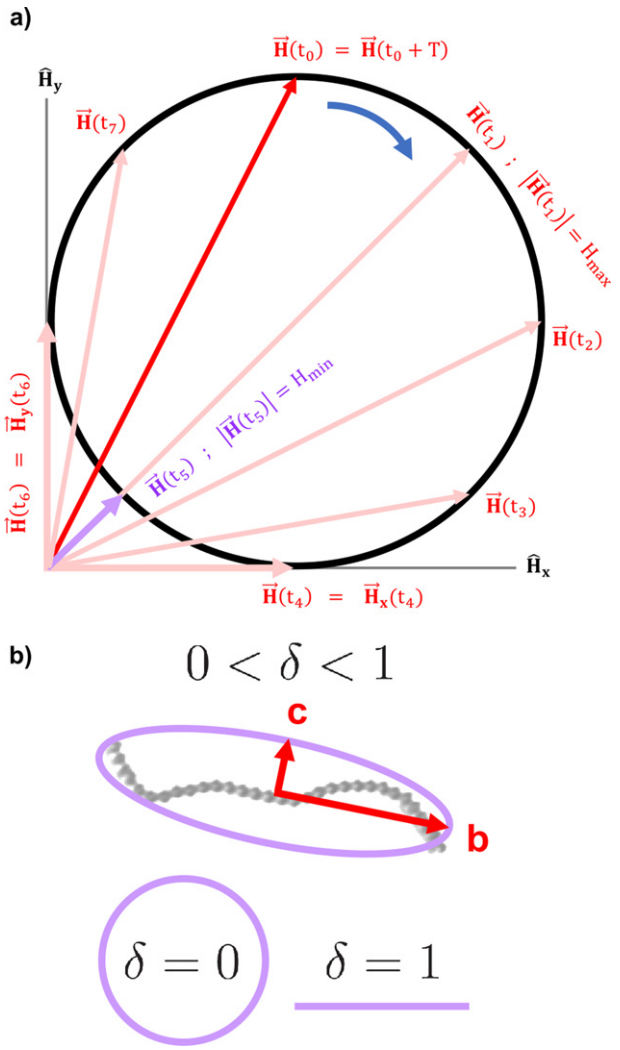

Figure 2. Schematics of the eccentric field and the chain asphericity. (a) Eccentric field with DC offsets $\lambda_x = \lambda_y = 1$. This choice of offsets constrains the rotation of the field to the first quadrant of the (H_x, H_y) plane. Both the magnitude and direction of the eccentric field change with time. The magnitude at each instant can be implied by the length of the arrows. The red arrow represents $\mathbf{H}$ at the beginning and end of a field period (t_0 and $t_0 + T$, respectively), where $T = 1/f$. As time proceeds, the magnetic field rotates clock-wise from t_0–t_7. Some instantaneous vectors of interest of the eccentric field include: $||\mathbf{H}(t_1)|| = H_{\max}$ where the field magnitude is maximum, $\mathbf{H}(t_4) = \mathbf{H}_x(t_4)$ at which the y-component of the field vanishes, $||\mathbf{H}(t_5)|| = H_{\min}$ where the field reaches its minimum magnitude, and $\mathbf{H}(t_6) = \mathbf{H}_y(t_6)$ at which the x-component of the field vanishes. The time instants t_1 through t_7 are arbitrary and used only to indicate progression. (b) Asphericity δ used as one of the parameters to monitor deformation. The eigenvalues, b and c, of the gyration tensor S_{nm} are used to determine δ. The eigenvalues represent the major and minor axes of the ellipse that best fits the shape of the chain. The value of δ is a measure of the compactness of the ellipse, varying between $0 < \delta < 1$. The limits of δ are a circle ($\delta = 0$) and a line ($\delta = 1$), corresponding to the least and most compact shapes, respectively. A straight chain has $\delta = 1$, so any decrease in this value monitors deformation by indicating that the chain becomes less compact relative to a straight line.

Therefore, the rotation of the eccentric field was confined to the first quadrant of (H_x, H_y), as shown in figure 2(a).

The rotation of the eccentric field can be visualized by starting at the tip of the red arrow in figure 2(a). This vector represents the magnetic field $\mathbf{H}$ at the beginning of the cycle ($t = t_0$). The length of the arrow indicates that it has a strong magnitude ($||\mathbf{H}|| > H_o$). As time progresses, the magnetic field rotates clockwise. Early in the cycle, the field strength rises until it reaches its maximum magnitude ($||\mathbf{H}(t_1)|| = H_{\max}$ in the schematic). Then, it decreases in magnitude as it continues to rotates, eventually reaching an instant at which the y-component of the field vanishes, so $\mathbf{H}(t_4) = \mathbf{H}_x(t_4)$ (at this time, its magnitude is $||\mathbf{H}|| = H_o$). After this time, the y-component becomes nonzero once again but the overall strength of the field continues to decrease (now $||\mathbf{H}|| < H_o$) until it reaches its minimum magnitude ($||\mathbf{H}(t_5)|| = H_{\min}$ in the schematic). Afterward, the magnitude increases and eventually the x-component of the field now vanishes while the y-component remains ($\mathbf{H}(t_6) = \mathbf{H}_y(t_6)$ and the magnitude is $||\mathbf{H}|| = H_o$ once more). Immediately after this point, the vanished component becomes nonzero again as the field continues to increase until it returns to its initial direction and magnitude at the end of the period ($T = 1/f$). Over the entire period, the magnetic field draws a circle whose center is not at the origin of (H_x, H_y). Our selection of $\lambda_x = \lambda_y = 1$ ensures that there are two instants at which one of the components vanishes while the other remains with magnitude equal to the amplitude H_o. If the offsets were set to values higher than unity, the circle formed over time by the field in the first quadrant would not have vectors parallel to the axes. If the offsets were chosen to be less than unity, the field would be able invert its direction and enter other quadrants. Video S1 (https://stacks.iop.org/CM/34/184005/mmedia) illustrates the eccentric field in action.

To apply the eccentric fields on the colloidal chains, a power supply (Agilent N6705A) generates currents that pass through two pairs of orthogonal iron-core coils. A function generator following equation (1) with user-selected frequency and voltage controls the power supply. The instantaneous magnitude and direction of the eccentric magnetic field are determined from the coils' voltage-field calibration curves. The magnetic field produced at the center of the coils is uniform, ensuring that the magnetic force acting on each particle is caused only by dipolar interactions with other particles and not by a gradient of the external magnetic field. The amplitude H_o was set to 4.3 or 5.9 kA m^{-1}, while f was varied from 0.01 to 2 Hz. All experiments were performed at room temperature.

2.3. Image acquisition

The sample cell was placed on a fixed stage located at the center of the coils. Chains made of 15–45 particles were tracked with a 40× objective and a CCD camera (Hamamatsu) recording at 9 frames per second. Before applying an eccentric field, the chains were initialized for experiments by subjecting them to a static field equal to equation (1) at $t = 0$. The dynamics of individual chains were recorded for several values of f and H_o. Video footage of each experiment consisted of 1000–3000 frames. The images were processed using a custom MATLAB code that performed Gaussian blurring, thresholding, morphological operations, and skeletonization. The particle positions are approximated from the skeleton of the chain using a moving average.

2.4. Chain analysis and deformation parameters

We examine every instant of the chain dynamics within a field period in terms of the ratio of viscous to magnetic torques and the global phase lag angle between the chain and field directions. The dimensionless viscomagnetic ratio γ is estimated as a Mason number that varies in time due to the nonconstant magnitude of the eccentric field

$$\gamma(t) = \frac{144\pi\eta f}{\mu_o \chi^2 ||\mathbf{H}(t)||^2} = \mathrm{Ma}\frac{H_o^2}{||\mathbf{H}(t)||^2} \tag{2}$$

where $||\mathbf{H}(t)|| = (||\mathbf{H}_x(t)||^2 + ||\mathbf{H}_y(t)||^2)^{1/2}$ is the instantaneous magnitude of the external field, η is the fluid viscosity, μ_o is the magnetic permeability of the vacuum, χ is the magnetic susceptibility of the particles, and Ma is the Mason number: $\mathrm{Ma} = 144\pi\eta f/\mu_o\chi^2 H_o^2$ [28, 42].

To determine the global phase lag angle, $\alpha(t)$, we calculate the components of the gyration tensor of the chain through time as [43, 44]

$$S_{nm} = \frac{1}{2N^2}\sum_{i=1}^{N}\sum_{j=1}^{N}(r_n^i - r_n^j)(r_m^i - r_m^j) \tag{3}$$

where N is the number of particles in the chain and r_n^i is the nth-component of the position vector of particle i. Note that the gyration tensor in equation (3) may be simplified to a 2×2 tensor because the dynamics of the chain are mostly confined to a 2D plane. Therefore, the orientation of the chain, $\theta(t)$, is defined by the direction of the principal eigenvector of S_{nm}. In this sense, $\alpha(t)$ is calculated from

$$\alpha(t) = |\phi(t) - \theta(t)|\,, \tag{4}$$

where the instantaneous direction of the magnetic field is $\phi(t) = \tan^{-1}[\mathbf{H}_y(t)/\mathbf{H}_x(t)]$.

Two geometric parameters are used to quantify the extent of deformation. The first one is the asphericity, which is commonly used to track structural changes in sheared polymers and is computed as [4, 44]

$$\delta = 1 - \frac{4bc}{(b+c)^2} \tag{5}$$

where b and c are the eigenvalues of equation (3). The asphericity δ can acquire values between 0 and 1. As $\delta \to 1$, the chain approaches a linear configuration, whereas lower δ indicates deviations from the straight line. Additionally, as δ decreases, the primary axis (b) shortens while the secondary axis (c) lengthens, making the chain less compact, as schematically shown in figure 2(b). As a second indicator of

deformation, the total bending energy for a discrete chain is computed as

$$U^{\mathrm{b}} = \frac{1}{2} k_{\mathrm{B}} T l_{\mathrm{p}} \sum_{i=2}^{N-1} \left(\frac{(\vartheta_{\mathrm{b}i})^2}{\Delta s_i} \right) \tag{6}$$

where l_{p} is the chain persistence length, k_{B} is the Boltzmann constant, T is the absolute temperature, i is the particle index which does not include the beads at the ends, $\vartheta_{\mathrm{b}i}$ is the angle between two adjacent segments connecting three neighboring particles, and Δs_i is the average arclength of the segments that form $\vartheta_{\mathrm{b}i}$. Equation (6) quantifies how much elastic energy is stored within the chain as it develops regions of curvature along its contour during deformation events.

3. Numerical simulations

To model the dynamics of the paramagnetic chains in the eccentric magnetic fields, a bead-spring model is used [45], in which N spherical beads with the same radius a have their centers connected by massless springs of length $l_0 = 3a$, giving the computational chain a total contour length of $L = 3a(N-1)$. Here, N was set to be 31 or 41 particles. The colloidal particles and dsDNA linkers represent the beads and springs, respectively. The suspending phase is assumed to be Newtonian with viscosity η. In the view of the characteristic small scale of the chains, the surrounding flow is governed by the Stokes equations, whereby the dynamics are inertia free. Non-local hydrodynamic interactions were only taken into account between the beads, ignoring the presence of the DNA and nearby walls. Thus, we formulate the problem using a mobility description, such that the velocity of the particles are a linear function of the non-hydrodynamic forces applied to the particles and their relative disposition in space,

$$\mathbf{v}_i = \sum_{j=1}^{N} \mathbb{G}^{ij} \cdot \mathbf{F}_j \quad \text{for } i, j = 1, \ldots, N; \tag{7}$$

where $\mathbf{v}_i$ is the velocity vector of the particle i; $\mathbf{F}_j$ is the force vector representing the sum of all non-hydrodynamic forces acting on the particle j; and $\mathbb{G}^{ij}$ is the mobility tensor of dimension 3×3 relating the dynamics of the particles i and j. For the present study, the Rotne–Prager mobility tensor is used to account for the particles' hydrodynamic interactions [46, 47],

$$\mathbb{G}^{ii} = \frac{\mathbf{I}}{6\pi\eta a} \tag{8}$$

and

$$\mathbb{G}^{ij} = \frac{1}{8\pi\eta} \left\{ \frac{1}{r} [\mathbf{I} + \hat{\mathbf{r}}\hat{\mathbf{r}}] + \frac{2a^2}{3r^3} [\mathbf{I} - 3\hat{\mathbf{r}}\hat{\mathbf{r}}] \right\} \quad \text{for } i \neq j, \tag{9}$$

where $\mathbf{r}$ is the distance vector between the center of the particles i and j, $r = |\mathbf{r}|$, and $\hat{\mathbf{r}} = \mathbf{r}/|\mathbf{r}|$.

The mechanical properties of the dsDNA linkers define the elastic properties of the chains, and therefore, their rigidity. We consider the stretching and bending elastic energies distributed through the chain, respectively defined as

$$u^{\mathrm{s}} = \frac{\sigma_{\mathrm{s}}}{2l_0}(r - l_0)^2 \quad \text{and} \quad u^{\mathrm{b}} = \frac{\sigma_{\mathrm{b}}}{2l_0}(\vartheta_{\mathrm{b}})^2, \tag{10}$$

where σ_{s} and σ_{b} are the stretching and bending moduli, and ϑ_{b} is defined as the angle between two adjacent segments connecting three neighboring beads. Hence, from a Hamiltonian perspective, the elastic forces acting on each particle j can be calculated as

$$\mathbf{f}_j^{\mathrm{s}} = -\nabla_j u^{\mathrm{s}} \quad \text{and} \quad \mathbf{f}_j^{\mathrm{b}} = -\nabla_j u^{\mathrm{b}}. \tag{11}$$

Throughout this work, we set $\sigma_{\mathrm{s}} = 4\sigma_{\mathrm{b}}/a^2$, following the Euler–Bernoulli beam-theory for a circular cross section assuming its radius as the one of the particles.

To account for the particles' magnetic interactions, we make use of the mutual dipole model as described in references [22, 26]. The magnetization $\mathbf{m}$ of the particles mutually interact with each other leading to

$$\mathbf{m}_i = \frac{4}{3}\pi a^3 \chi \left[\mathbf{H}(t) + \sum_{j \neq i}^{N} \mathbb{M}^{ij} \cdot \mathbf{m}_j \right], \tag{12}$$

where $\mathbb{M}^{ij} = (3\mathbf{rr}/r^5 - \mathbf{I}/r^3)/4\pi$ is known as the grand potential tensor [48]. Equation (12) leads to a linear system of equations whose solution gives the particles' magnetic moments. Once the magnetic moments are computed for a determined spatial configuration, the magnetic force for each particle is calculated using

$$\mathbf{f}_i^{\mathrm{mag}} = -\sum_{j \neq i}^{N} \frac{3\mu_0}{4\pi r^5} \left[(\mathbf{m}_i \cdot \mathbf{r})\mathbf{m}_j + (\mathbf{m}_j \cdot \mathbf{r})\mathbf{m}_i + (\mathbf{m}_i \cdot \mathbf{m}_j)\mathbf{r} - 5\frac{(\mathbf{m}_i \cdot \mathbf{r})(\mathbf{m}_j \cdot \mathbf{r})\mathbf{r}}{r^2} \right]. \tag{13}$$

To avoid nonphysical configurations and singularities related to the hydrodynamic formulation, we account for the contact interaction between two beads following the hard-sphere description for two spherical bodies. The elastic modulus and Poisson's ratio of the particles were empirically chosen to minimize particle interpenetration and also avoid numerical instabilities.

The non-dimensionalization of the problem is done using L for length, f^{-1} for time, H_o for the magnetic field strength, and $4\pi a^3 \chi H_o$ for the particles' magnetic dipoles. In this sense, we get that the dynamics of the paramagnetic chains are defined by two dimensionless groups. The first is the Mason number, Ma, representing the ratio of viscous to magnetic forces using the constant amplitude H_o, as defined in equation (2). The second dimensionless group is the magnetoelastic number Mn defined as [49]

$$\mathrm{Mn} = \frac{\pi a^2 \mu_o H_o^2 L^2}{6\sigma_{\mathrm{b}}} \frac{\chi^2}{(1 - \chi/6)(1 + \chi/12)}. \tag{14}$$

The simulations allow us to probe more conditions of Mn and Ma than would be possible with experiments. Notice that for the numerical simulations we neglect the role of Brownian motion in the chain dynamics.

4. Results and discussions

4.1. Time series of the deformation parameters and characteristic chain morphologies

In both experiments and simulations, a colloidal chain under an eccentric field displays novel periodic dynamics consisting of a steady cycle of deformation and stretching events during the partial rotation of the chain, as illustrated by the pulses in the time series of the chain's asphericity δ and total bending energy U^{b} in figure 3. The deformation of the chain is quantified by both the decrease of δ and the accompanying increase in U^{b}. The decrease in δ signifies the adoption of a less compact shape compared to a stretched chain, as visualized in figure 2(b), whereas the increase in U^{b} indicates the development of curvature along the backbone. Recovery of the straight chain configuration occurs immediately after δ and U^{b} reach their minimum and maximum values, respectively, as seen by the subsequent rise $\delta \to 1$ and drop-off $U^{\mathrm{b}} \to 0$. The time interval between consecutive pulses of both quantities in experiments is consistent with the period of rotation of the eccentric field, while in simulations the pulses are separated by a dimensionless interval equal to 2π, thereby confirming the periodic nature of these dynamics.

Subtle, albeit important, features of these deformation dynamics are detected in the time series of the deformation parameters as the frequency of the eccentric field is changed. These details are associated to the bending of the chains into distinct characteristic morphologies that vary in curvature and in their number of bending modes (arches). Therefore, the chain can attain different shapes during its deformation that depend on the frequency. When operating at low field frequencies (or low Ma) like in figures 3(a) and (b), the main feature of the dynamics is the simultaneous occurrence of the peaks of the pulses of δ and U_{b}, indicating that the less compact configuration acquired by the chain is also the configuration with the highest curvature. In these cases, the chain progressively bends into an S-like configuration (figure 4(a) and videos S2–S3) that satisfies both of these properties. This S-shape is akin to how other elastic paramagnetic and ferromagnetic colloidal chains bend under conventional circular magnetic fields [30, 32]. However, the S-shape of the chains in the low-frequency circular field is a steady state configuration during the rotational dynamics. In contrast, under the eccentric field, the S-shaped chain stretches back to its linear configuration and proceeds to repeat the sequence of bending and stretching.

At intermediate frequencies, the depth and height of δ and U^{b}, respectively, become more pronounced as seen in figures 3(c) and (d). Therefore, the chain deforms much more compared to the lower frequency cases. Furthermore, there is now a delay between the peaks of the parameters. The chain first reaches its minimum in δ, and then U^{b} becomes a maximum once $\delta \to 1$. Interestingly, the pulses start and finish at the same time despite the delay in their peaks because they are asymmetric (see the insets of figures 3(c) and (d)). The delay between deformation peaks indicates that at intermediate frequencies (or intermediate Ma) the configuration that is less compact is not the same as the configuration with highest curvature. In fact, the chain shapes corresponding to each peak differ significantly. The peak in δ corresponds to a very open S-shape. More importantly, a new morphology occurs at the peak of U^{b}. It consists of another two-arched structure whose curvature becomes highly localized at the center of the chain, while the chain ends resemble two long straight lines well aligned with the instantaneous magnetic field (see figure 4(b) and videos S4–S5). Such attributes make for a very compact shape (δ not small) with significant elastic energy stored at the center. We refer to this morphology as the Z-shape, which is the characteristic shape observed at intermediate frequencies. Note that the open S-shape is a necessary precursor for the formation of the Z-shape.

Increasing the frequency further leads to another characteristic morphology of the chain with its own distinct features in the periodic dynamics. The first feature is that the peaks of both deformation parameters become less pronounced compared to the intermediate frequency scenario, as shown in figures 3(e) and (f). Hence, the chain configurations obtained at higher frequencies are once again less compact and less bent compared to the Z-shape scenario. In these frequencies, the chain bends into a four-arched structure, as depicted in figure 4(c) and videos S6–S7, instead of a two-arched configuration like in lower frequencies. We refer to this shape as '4-mode'. The observations from all cases in figure 3 suggest that the deformation is maximized at intermediate frequencies. A detailed analysis of the frequency-dependence of the peaks of the deformation parameters will be presented in section 4.3.

The second feature observed in the dynamics at higher frequencies is that the delay between the deformation peaks decreases as the frequency increases, leading to situations in which the peaks of both parameters occur simultaneously. In fact, the chain displays the 4-mode configuration at this instant, as seen in the upper inset of figure 4(c). As the frequency continues to increase, the peak values become less pronounced and the delay between deformation peaks appears once again but the order of each peak is inverted: now U^{b} reaches its maximum first, while δ reaches its minimum once U^{b} is already descending. In figures 3(e) and (f) and 4(c), we show cases from experiments and simulations that display the inverted order in the delay. Note from the insets of figures 3(e) and (f) that both pulses still start and end simultaneously. In these insets, the shape of the experimental pulse differs qualitatively from the simulation because its width is too small to acquire sufficient sampling with the frame rate of the camera. Finally, the third feature of these dynamics is the presence of small secondary peaks in δ between the main peaks. The secondary minima of δ suggest that the chain deflects subtly prior to undergoing the main deformation event. With increasing frequency, the depth of this peak becomes slightly more pronounced, enhancing this initial deflection. The simulations also showcase a small peak in U^{b} simultaneous to the small peak in δ, but we cannot distinguish this peak from noise in our experiments. Regardless, the results from both experiments and simulations show very good agreement in most of the attributes of the periodic dynamics.

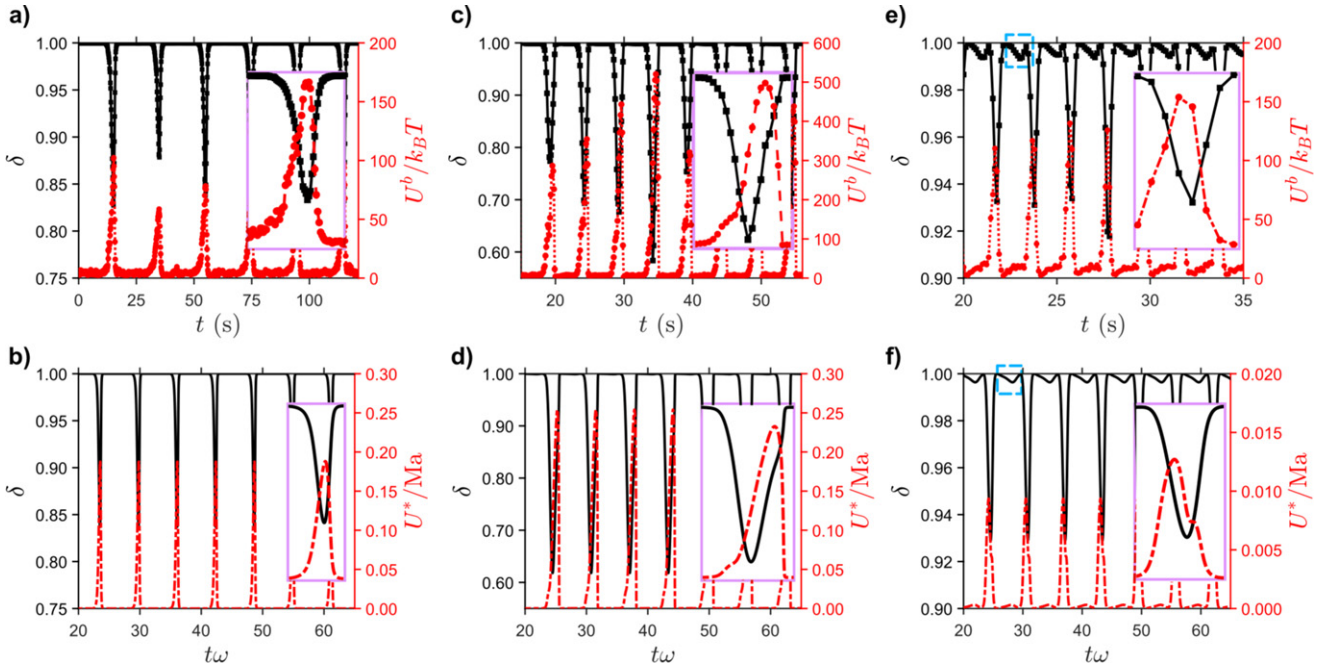

Figure 3. Time series of the deformation parameters δ (asphericity) and U^{b} (bending energy) showcasing the periodic deformation dynamics of the chains in an eccentric field. Pulses indicate deformation and relaxation. The time between each pulse corresponds to the field period ($T = 1/f$ for experiments, 2π for simulations). Top panels: experiments ($N = 34$ particles, $H_o = 4.3$ kA m^{-1}). Bottom panels: simulations ($N = 31$, Mn $= 300$). Dynamics at (a) $f = 0.05$ Hz and (b) Ma $= 0.0008$ corresponding to an S-shape morphology. Insets show peaks of δ and U^{b} occurring simultaneously. Dynamics at (c) $f = 0.2$ Hz and (d) Ma $= 0.0050$ corresponding to a Z-shape. Peak values become more pronounced compared to S-shape. Insets: peaks show a delay, δ reaches its minimum before U^{b} reaches its maximum. Dynamics at (e) $f = 0.5$ Hz and (f) Ma $= 0.01300$ corresponding to a 4-mode structure. Peak values become less pronounced compared to Z-shape. A secondary but small peak also appears (enclosed by the blue dashed boxes). Insets: peak values are still delayed but the order has inverted. Note that the bending energy in simulations is dimensionless: $U^* = 12U^{\mathrm{b}}/a\pi L^2\mu_o\chi^2H_o^2$.

The Z-shape and the 4-mode structure are new nonequilibrium configurations that have not been observed in previous studies of magnetic filaments exposed to time-varying fields while immersed in a viscous fluid. These morphologies are similar to the buckled states acquired by long chains under an orthogonal static field, but the structures in those cases are in a local equilibrium and hence do not change after a coarsening time because the magnetic field stays constant [41]. We emphasize then that the novel characteristic morphologies are transitory within the field period. It should be clarified that a transient 4-mode shape was also reported by Huang *et al* under a circular field [50], but the process was considerably different because the particles constituting their chains were unlinked and embedded within an elastomer matrix that hindered rotation in the circular field to propitiate buckling instabilities. The mechanism by which the eccentric field causes the deformation of colloidal chains will be described in section 4.2.

Therefore, the eccentric fields not only reveal novel dynamics involving periodic bending and stretching of these semiflexible colloidal systems, but also propitiate the formation of new morphologies when operating at particular field parameters. These novel periodic dynamics of the structure of colloidal chains in eccentric fields are reminiscent of the stretch–coil transitions observed during the alignment and tumbling of actin filaments under shear flow [3, 4, 51, 52]. The changes in configuration are coupled to the orientation of the chain, which depends on the instantaneous strength and direction of the magnetic field. The intricate relationship between the instantaneous magnetic field and the chain orientation on the deformation dynamics will be discussed in detail next.

4.2. Stages of the chain dynamics

Before delving into our analysis, we will summarize relevant background on the rotational dynamics of rigid colloidal chains that will be useful to build our explanation of the semiflexible chains' behavior in eccentric fields. During the rotation of an external time-varying field, rigid chains experience a driving magnetic torque that attempts to bring them to equilibrium by aligning their long-axes with the direction of the field. Considering a simple dipolar model, this phenomenon arises because the pair dipolar interactions among the constituent particles scale with the phase lag angle α as $U_{ij}^d \sim ||\mathbf{H}||^2(1 - 3\cos^2\alpha)$, so the total energy is minimized when the chain has the same orientation as the field [53, 54]. However, the opposing viscous torque prevents minimization of the phase lag, leading to rotational dynamics that depend on the parameters of the external field. Under a conventional circular field, a simple torque balance yields a model for the time-evolution of α as a function of the relative strength between magnetic and viscous torques [55, 56]. In contrast, the time-varying magnitude of the eccentric field used in this study complicates the prediction of the phase lag. Furthermore, the

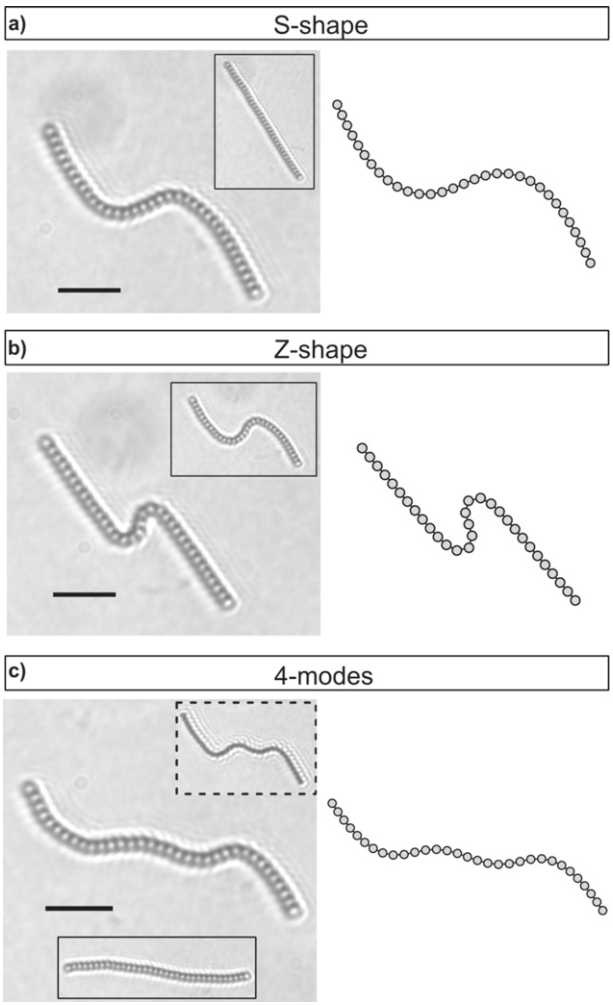

Figure 4. Characteristic chain morphologies under an eccentric field. Left: microscopy images of a chain with $N = 34$ particles at $H_o = 4.3$ kA m^{-1} under different frequencies. Right: configurations obtained from numerical simulations for a chain with $N = 31$ particles having Mn $= 300$ under different Ma. (a) S-shapes form at low frequencies (Left: $f = 0.05$ Hz. Right: Ma $= 0.0008$). This morphology corresponds to the simultaneous peaks of the deformation parameters in the time series. Inset: linear configuration after the chain stretches. (b) Z-shapes are very compact structures with very pronounced curvature at their center (Left: $f = 0.02$ Hz. Right: Ma $= 0.0050$). This shape appears at intermediate frequencies and corresponds to the delayed peaks in U^{b}. Inset: intermediary S-shape that has the smallest δ for these dynamics and that quickly coarsens into the Z-shape. (c) The chains fold into four-arched wave configurations at higher frequencies (Left: $f = 0.5$ Hz. Right: Ma $= 0.01300$). This configuration is the most bent in the cycle, but not the most compact. Lower inset: deflected chain that manifests as the small peak of δ in the time series. Upper inset: 4-mode morphology for $f = 0.3$ Hz that is the most bent and also the least compact configuration in its cycle. Note: simulation images have been rotated to match the field axes of the experimental images. Scale bars: 10 μm.

semiflexible nature of our chains implies that the local phase lags (α_{ij}) between each pair of particles along a chain can differ significantly from the global lag (α) because the free ends of the chain can follow the field with less resistance than the center [26, 57]. Therefore, the pair potential felt by each particle is different according to its position along the chain contour, altering the magnetic force and torque that act on each of them.

Despite the multiple local phase lags and the nonconstant magnitude of the eccentric field, the global phase lag α and the instantaneous viscomagnetic ratio γ (equation (2), which is equivalent to a Mason number with nonconstant $||\mathbf{H}||$) can still be useful indicators of the overall state of the dipolar interactions along the semiflexible chain and the torque on the filament, respectively. For instance, a small global α can be associated to overall attractive interactions ($U_{ij}^d < 0$) whereas a large α can be indicative of repulsive interactions ($U_{ij}^d > 0$). Moreover, small γ are indicative of a strong magnetic torque acting on the chain, while for large γ the viscous drag dominates. In turn, α provides information about the dipolar interactions, which can be related to changes in the chain morphology over the field period. Therefore, in this section we describe how the behavior of γ correlates with the global α of the chain (computed from equation (4)) at each point in time within a single period of the eccentric field dynamics. Overall, this description explains how the instantaneous direction and magnitude of the eccentric field are related to the deformation parameters that quantify the development and relaxation of the characteristic morphologies in the periodic dynamics. The entire pattern in a period can be decomposed into four stages of motion that are consistent for the three characteristic morphologies, albeit with some deviations for the 4-mode shape. Figure 5 showcases an example from experiments (after image processing) of the four stages for the case presented in figure 4(b): a chain of $N = 34$ particles deforming into a Z-shape at $f = 0.2$ Hz and $H_o = 4.3$ kA m^{-1}.

Stage I of the dynamics is characterized by having large field magnitudes ($||\mathbf{H}|| > H_o$) and displaying chain rotation. These two traits can be readily seen in the first-row panels of figure 5(a). Due to the large field magnitude, the values of γ are the smallest during this portion of the cycle, as shown in figure 5(b). This means that the magnetic torque dominates over the viscous drag during stage I. Consequently, the driving torque is sufficient to induce rotation of the chain at overall small α. Such small α indicate that the dipolar interactions between the particles can be considered attractive. Therefore, the chain maintains an overall straight shape, having $\delta \sim 1$ and $U^{\mathrm{b}} \sim 0$ as previously discussed and highlighted once again in figure 5(c). The attraction between the particles is emphasized by the dark blue coloring of the points in the chain skeleton (figure 5(a)), representing small local phase lags α_{ij} that do not deviate considerably from each other. We should remark that although the field magnitudes are large, they are also of decreasing strength throughout most of this part of the cycle, leading to the small increases in α. The stage lasts for about half of the field period and ends when the field reaches $\mathbf{H} = \mathbf{H}_x$ (hence, $||\mathbf{H}|| = H_o$).

In stage II, the rotation of the chain halts due to the significant decrease in the magnitude of the field. Within this portion of the cycle, $||\mathbf{H}||$ decreases from H_o to H_{min} (corresponding to about 1/8 of the period), so the value of γ rises rapidly until

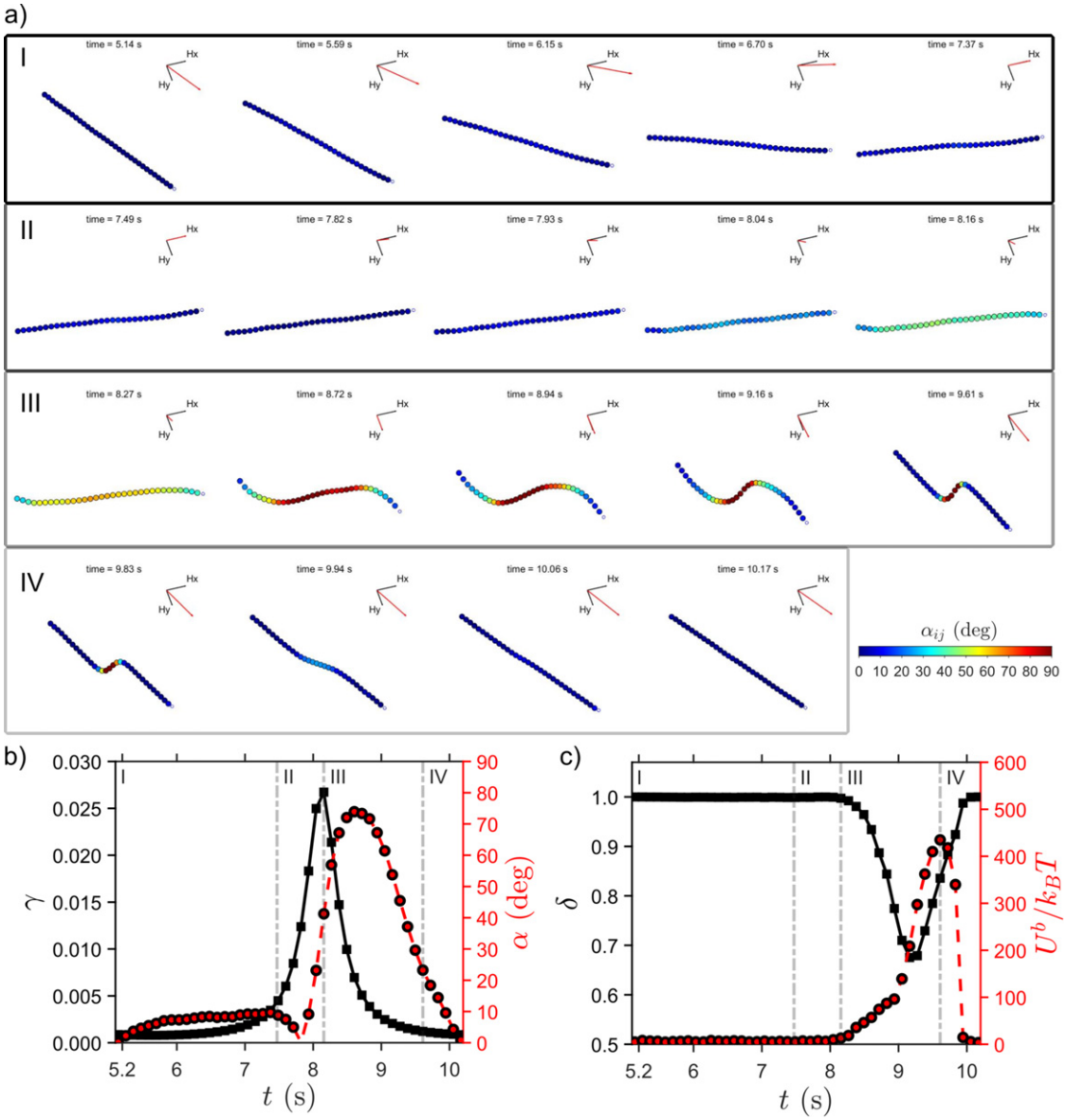

Figure 5. Four stages of the dynamics for a chain of $N = 34$ particles deforming into a Z-shape at $f = 0.2$ Hz and $H_o = 4.3$ kA m^{-1} (a) Panels showcasing the configuration and orientation of the chain at representative instances of each stage. The images come from experiments and have been processed to highlight the local α_{ij} at each point along the chain. Each panel indicates the axes of the magnetic field components in the frame of the images. The red arrows starting from each axes represent the instantaneous direction and magnitude of the eccentric field. (b) Time-varying viscomagnetic ratio γ (black squares, solid line), global α (red circles, dashed line) of the chain, and (c) deformation parameters δ (black squares, solid line) and U^{b} (red circles, dashed line) over time within a single period of the field. Boundaries between the four stages are highlighted.

it reaches its maximum. Therefore, the viscous drag becomes dominant over the magnetic torque and the chain stops rotating, as seen by negligible changes in orientation in the second-row panels of figure 5(a). Although the chain rotation stops, the value of α keeps changing: it first drops to zero and then increases again (figure 5(b)). This behavior in the phase lag is caused by the weak magnetic field changing its direction while not being strong enough to induce changes in the orientation of the chain. For S-shape and Z-shape morphologies, there are no significant changes in the deformation parameters of figure 5(c) up to this point. At the latter instants of this stage, the field reaches its weakest magnitudes in the cycle and also the global α increases considerably, allowing for small deflections on the ends of the chain to emerge. This deflection can be observed by the changes in coloring of the local α_{ij} along the chain skeleton. These phase lags indicate that the dipolar interactions, while still attractive, are not strong enough to maintain a straight configuration [58]. The rise of the global α and the development of significantly different local angles α_{ij} throughout the chain are crucial for the onset of the deformation into the characteristic morphologies in the next stage. The reason is that it positions the chain far from alignment in a field that will subsequently increase rapidly in magnitude during the next stage.

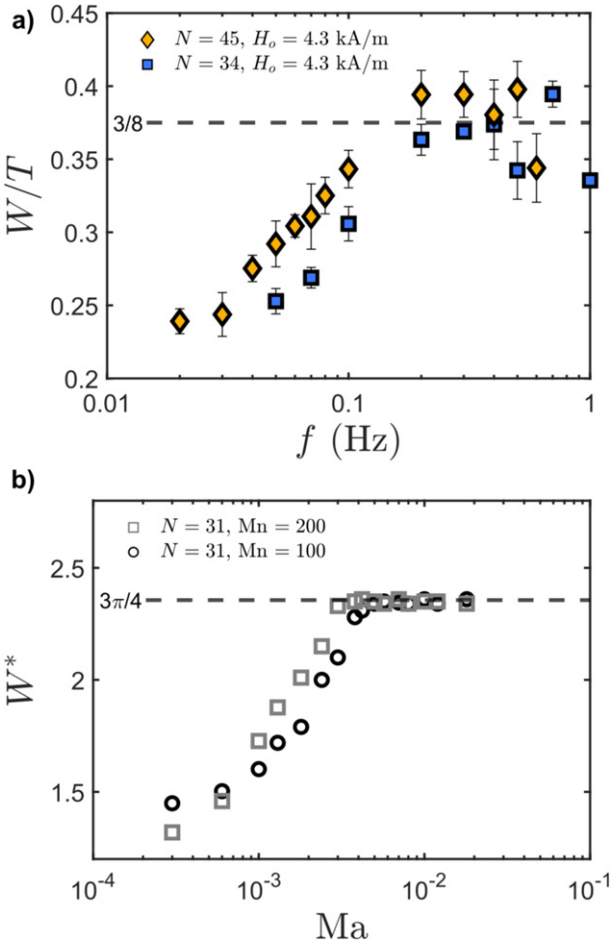

Figure 6. The duration of the pulse width (W) in each period reaches a plateau value. (a) Experiments: the ratio W/T, where the field period is $T = 1/f$, approaches $3/8$ as f is increased. (b) Simulations: the dimensionless pulse width (W^*) approaches $3\pi/4$ as Ma increases, since the dimensionless period is 2π. Therefore, at high frequencies, the pulse of a cycle lasts for $3/8$ths of the field's period. In these cases, as soon as the chain stretches back to the linear configuration, the cycle ends and stage I begins once more. For low frequencies, stage IV continues after the chain straightens because the chain needs to rotate to recover its initial orientation from which stage I restarts.

Stage III showcases the richest behavior because it is within this part of the cycle that the chain deforms into one of the characteristic morphologies. This stage begins when γ starts descending from its highest value (figure 5(b)). Although the decreasing γ means that the magnetic torque is becoming dominant once again, it is still not high enough to sustain rotation of the entire chain, particularly the regions closest to the center. Instead, the global α continues to increase mostly due to the rotation of the field. After reaching its maximum, α starts to decrease, but it still has overall large values, indicative of strong repulsive interactions along the chain as the field magnitude rises. Simultaneously, the small deflection at the tips begins to propagate inward. The propagation of this bending wave is a consequence of progressively longer portions of the chain at the free ends aligning with the direction of the increasing field. In contrast, the center of the chain remains orthogonal to the field. Therefore, the free ends experience attractive interactions while the central segment is highly repulsive. The strong magnetic repulsion overcomes the bending rigidity of the chain, so the curvature of the propagating deflection increases. Overall, this process leads to the formation of an S-shape. The attraction at the ends and the repulsion at the center are emphasized by the blue and red regions of the local α_{ij} along the chain illustrated in the third-row panels of figure 5(a). If the frequency is small, γ will become low enough during its descent while the mild S-shape is developing, so the increasing magnetic torque and the attractive interactions at the end segments will drive the restraightening of the chain before the curvature grows too much, marking the end of stage III.

The transition from an S-shape to a Z-shape as the frequency is increased from low to moderate values can be elucidated from this analysis. Stage III in figure 5(a) shows that at an intermediate frequency, a precursory S-shape is formed, similar to that observed at the low frequencies, with overall γ values that are larger. Since the viscous drag dominates over the magnetic torque, the innermost particles of the chain become even more misaligned with the field, compared to the progressively longer and more aligned end segments. Then, the continuous increase in field strength causes the repulsive dipolar interactions between the misaligned particles in the center to become even stronger. The mismatch between strongly repulsive particles in the center and strongly attractive particles in the ends leads to growth in the curvature of the traveling wave, resulting in the sharp bend that defines the Z-shape.

The propagation of bending waves (the deflection) proceeds until U^{b} reaches its peak (figure 5(c)). Since the deformation parameters have a delay between their peaks in the case of Z-shapes and 4-mode structures, we consider that stage III ends whenever U^{b} reaches its peak, regardless if it does so before δ. The reason we define the ending of stage III in this fashion is that if the peak in δ occurs afterward (for 4-mode morphologies), the chain has already started to stretch. Therefore, stage III corresponds to the portion of the eccentric field between the minimum field magnitude and the peak in U^{b}.

In the final stage (stage IV), the chain rapidly releases the stored elastic energy to relax back into the straight configuration. At this point, the field magnitude becomes large once again. The increased magnetic torque and the accompanying stronger dipolar attractions between the long segments make the deformed structure unfavorable. Consequently, the linear segments rapidly thrust outward as they attract each other and realign into a single linear shape, decreasing the global α. Depending on the frequency, the chain can either recover its linear configuration and then continue to rotate until it returns to its initial orientation when the field period ends (for S-shapes), or the instant at which it completes the stretching process matches the end of the period (for Z-shapes and 4-modes). This means that the pulse of the deformation parameters can end prior to or simultaneously with the conclusion of the field period. Therefore, the width of the deformation pulse in each cycle lasts $W \leqslant 3T/8$, approaching $3T/8$ as f increases. This behavior in the pulse width is confirmed in figure 6. Note that the period in the simulations

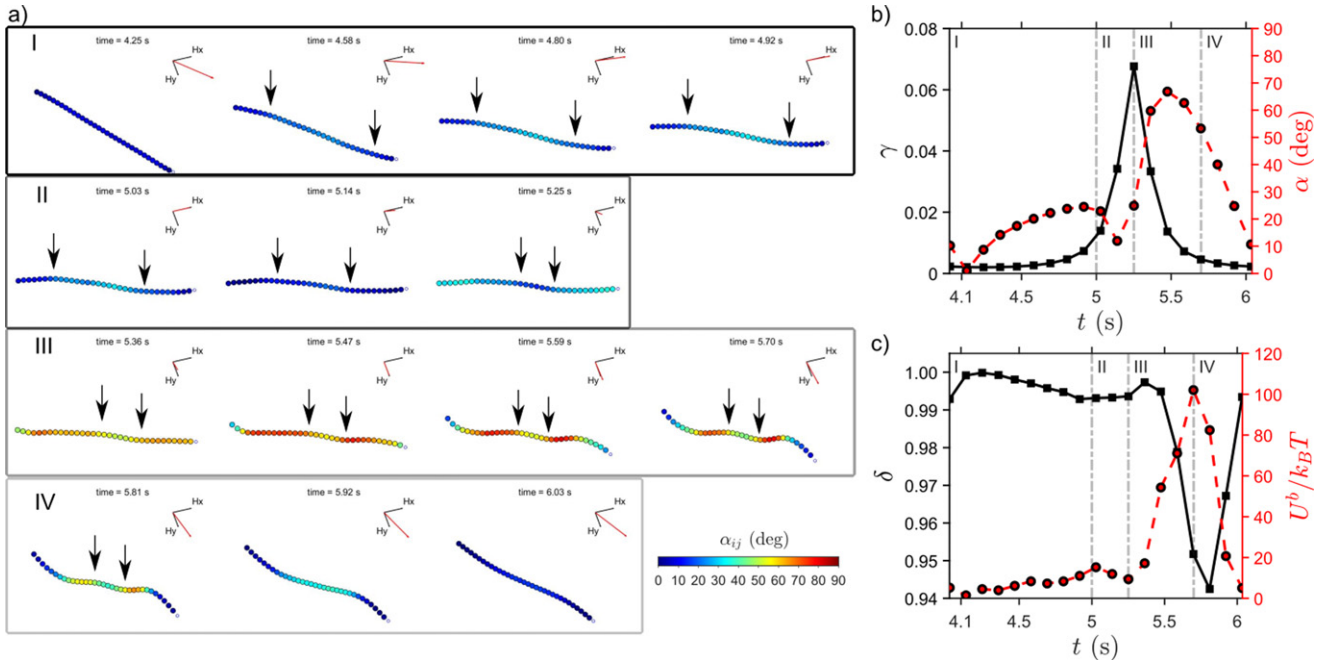

Figure 7. Stages of the dynamics for a chain deforming into a 4-mode structure ($f = 0.5$ Hz and $H_o = 4.3$ kA m^{-1}). The main difference with respect to figure 5 is the deflection that occurs in stage I and that persists throughout stages II and III. (a) Representative panels showing the configuration and orientation of the chain in the four stages. Black arrows above the chains point to the curvature that arises from the first deflection and that eventually grows into the inner arches of the 4-mode morphology. Color map represents local α_{ij}. Segments between adjacent inner and outer arches are almost orthogonal to the field direction. (b) Time-varying viscomagnetic ratio γ (black squares, solid line) and global α (red circles, dashed line) of the chain, and (c) deformation parameters δ (black squares, solid line) and U^{b} (red circles, dashed line) over time within a single period of the field. Boundaries between the four stages are highlighted.

is 2π, so the dimensionless pulse width is $W^* \leqslant 3\pi/4$. This finding demonstrates that we have identified the maximum duration of the deformation and relaxation process of the chain in an eccentric field. Once the straight chain returns to its initial orientation, the entire cycle encompassing the stages of rotation, arrested motion, deformation, and stretching restarts.

The above analysis describes quite well the behavior of the chain at conditions that lead it to deform into an S-shape or Z-shape. In the case of the 4-mode structure, however, there are some important differences that must be addressed. As previously discussed, one of the features of the 4-mode shape is the appearance of a small secondary peak in the time series of the deformation parameters (figures 3(e) and (f)) that corresponds to a deflected shape (bottom inset of figure 4(c)). This slight deflection is not trivial. In fact, it is crucial for the development of the additional arches in the 4-mode structure that differentiate it from the S and Z-shapes. Nonetheless, the characteristics of each stage are still the same as for the other morphologies. Figure 7(a) shows that the deflected state develops in stage I as the chain rotates. The origin of this deflection is the increased viscous torque experienced by the chain when operating at higher frequencies. Hence, even though γ is smallest during this part of the cycle, its values are higher compared to the case shown in figure 5. This implies that the magnetic torque is not strong enough to maintain an overall straight shape [37, 57], so the deviation in local α_{ij} between the free ends and the center becomes more pronounced in stage I. This is noticeable when looking at the color gradient of the local α_{ij} along the chain in the first-row panels of figure 7(a) and the higher values of global α presented in figure 7(b) compared to figure 5(b). However, the chain is still able to rotate at these values of γ, so stage I remains clearly defined. The curvature of the deflection also propagates inward without growing substantially.

During stage II of the 4-mode structure, the rotation of the chain is halted just like for the other morphologies. However, the shape remains deflected as the bending wave continues to propagate inward without significant coarsening in its curvature. Subsequently, in stage III, the free ends of the chain begin to deflect in the direction opposite to the one of the deflection seen in stage I. This initially leads to a more compact shape, as seen in the first panel of the third row in figure 7(a). Therefore, the small peak of δ decays (figure 7(c)). However, this resulting shape is not completely straight. The first deflection remains as small curved regions located close to the center of the chain. Then, as the field increases in magnitude and the global α rises (mostly due to the field's rotation), the second deflection propagates inward and coarsens into the outer arches of the 4-mode structure. Simultaneously, the small curvature from the first deflection also becomes more pronounced due to the increasing repulsive interactions, growing into the inner modes of the 4-mode morphology. This process culminates in the 4-mode structure that stores the highest bending energy during the cycle. This configuration marks the end of stage III. Finally, the 4-mode structure returns to the initial straight configuration in stage IV. To stretch, the inner modes relax faster than the outer arches as the dipolar interactions become more attractive and the magnetic torque dominates over the

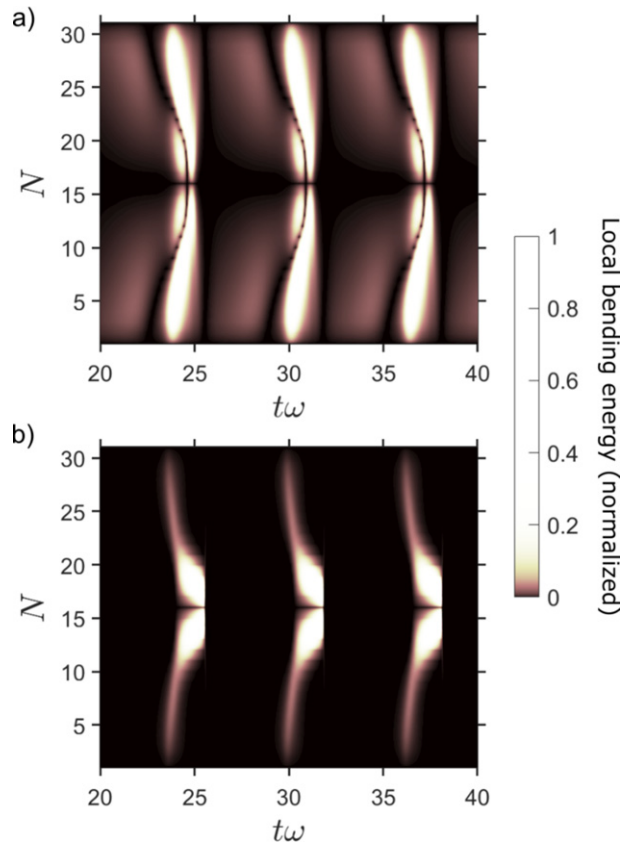

Figure 8. Spatiotemporal maps of the local bending energy obtained from simulations of chains with 31 particles. Each map shows three periods of the dynamics. N corresponds to the particle number along the chain. (a) 4-mode structure (Ma = 0.01300, Mn = 300): low energy regions that correspond to an initial deflection propagate over time and grow into the inner arches of the characteristic morphology. (b) Z-shape (Ma = 0.0050, Mn = 300): no deflections are observed prior to the onset and coarsening of the two arches. Local bending energies have been normalized by the maximum value of each case. A nonlinear colormap is used to emphasize regions of low local bending energy. Black regions represent straight segments.

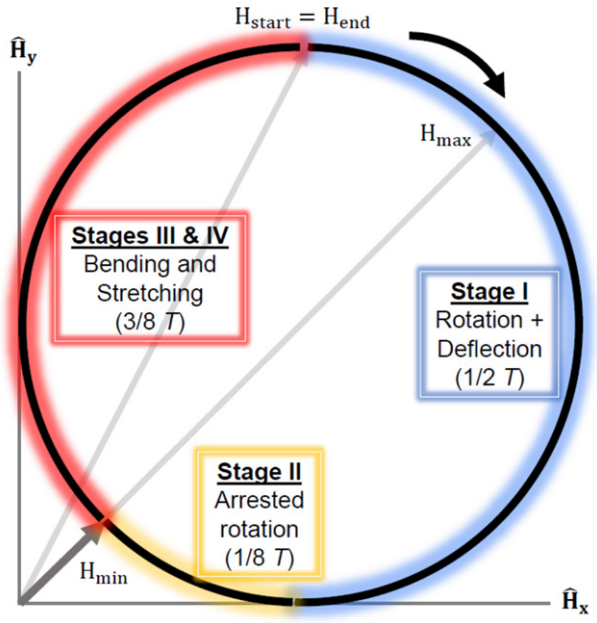

Figure 9. Schematic of the eccentric field's period divided into the four stages of the chain dynamics. Stage I is highlighted in blue. It is the longest stage and accounts for about 1/2 of the period. Within this stage, the chain rotates and it can deflect at its free ends if the Mason number is high enough. Highlighted in yellow is stage II, which corresponds to about 1/8 of the cycle. Here, the chain rotation stops but the external field continues to rotate. Stages III and IV are highlighted in red as the remaining 3/8 of the period. They encompass the deformation and straightening events, respectively, and account for the pulse of the deformation parameters in each cycle. The duration of stage III varies according to the Mason number, so the ending of this stage is not clearly defined within the circle. The width of the pulse of the deformation parameters can last the entire time highlighted by the red region, as demonstrated by the plateaus in figure 6. The chain reorients to its initial direction at the end of stage IV, thereby restarting stage I.

drag to realign the chain. The relaxation events are evident in the fourth-row panels of figure 7(a).

The observations from these dynamics reveal that the initial deflection arising in stage I is the source of the inner modes that develop in stage III (figures 3(e) and (f) and 7(c)). This origin is further confirmed by visualizing the local bending energy along the chain in a spatiotemporal map. Results from numerical simulations are used to generate this map because the sampling rate of the experiments does not provide enough resolution to accurately track the evolution of the localized bending energy. In figure 8(a), three cycles of the dynamics are shown. At the beginning of each period, low-intensity local bending energy bands are seen propagating inward with time. These bands correspond to the deflection of stage I that then persists throughout stage II. As these bands propagate, they first decrease in intensity as the chain initially acquires a less compact configuration (similar to the first panel of the third row in figure 7(a)) and then their intensity increases significantly close to the center of the chain. These brighter spots correspond to the inner modes, indicating that indeed the initial deflection evolves into the inner arches of the 4-mode configuration. This formation process of a four-arched structure is different from the transient buckling of unlinked chains immersed in an elastic medium under a circular field [50]. Moreover, figure 8(a) also shows that the inner modes relax prior to the outer arches, agreeing with the experimental images in the fourth row of figure 7(a). As a comparison, figure 8(b) shows the same spatiotemporal map for a Z-shape. Here, there are no low-intensity bands prior to the appearance, propagation, and coarsening of the bending waves that represent the two arches of the Z-shape.

While we have not performed a stability analysis of the chains in the eccentric field due to the complexity of the problem, the three characteristic morphologies visually resemble the sinusoidal shapes of magnetoelastic colloidal chains [41, 49, 50, 59, 60] and much larger magnetoelastic rods [61–63] undergoing higher-order buckling bifurcations under an orthogonal static field. For a chain to undergo higher bifurcations in such scenarios, the magnitude of the static field must be increased above progressively higher critical values that will favor the development of additional arches on the

chain backbone. In contrast, the bifurcations under an eccentric field occur as the frequency is changed. The S-shape arises at low frequencies because the straight configuration of the chain becomes unstable during stage III of the dynamics. Moderate frequencies then render the non-compact S-shape into the very compact sharp bend of the Z-shape. It would seem then that at higher frequencies the 4-mode structure is the result of another bifurcation. However, the classification of this shape as a bifurcation of the Z-shape is not straightforward because the inner and outer arches of the 4-mode configuration emerge from two distinct dynamical stages (stages I and III), as seen in figures 7 and 8(a).

Figure 9 summarizes the four stages of the chain dynamics by highlighting when each of these intervals occur within the period of the eccentric field. This analysis has revealed that the characteristic morphologies observed under an eccentric field arise due to the propagation and coarsening of bending waves during stage III. The bending waves originate as deflections caused by the intricate interplay between magnetic and viscous torques. The deflections then grow as the misorientation between the chain and the field increases because strong dipolar repulsion dominates over the flexural rigidity. The previous stages of rotation and arrest are crucial for the onset of the periodic deformation because they bring the chain to an orientation that favors large viscous drag and large repulsion.

4.3. Scaling analysis of the deformation parameters

Having elucidated the dynamics of the semiflexible chains in eccentric fields, we proceed to understand the impact that the field parameters and chain properties have on the extent of the deformation. In section 4.1, the peaks of bending energy and asphericity ($U^{\mathrm{b}}_{\mathrm{max}}$ and δ_{min}) seemed to become more pronounced at intermediate field frequencies. To elaborate on this observation, the average peak of the bending energy ($U^{\mathrm{b}}_{\mathrm{max}}$) for different chains is calculated at various f and H_o (experiments) or Ma and Mn (simulations). Figures 10(a) and (b) present $U^{\mathrm{b}}_{\mathrm{max}}$ as a function of scaled frequencies. The scaling is performed in terms of the critical magnetoviscous frequency (f_{c}) for experiments and its equivalent critical Mason number (Ma_{c}) for simulations, which are determined by [26, 31]

$$f_{\mathrm{c}} = \frac{\mu_o \chi^2 H_o^2 \ln\left(\frac{N}{2}\right)}{32\pi\eta N^2}, \tag{15}$$

$$\mathrm{Ma}_{\mathrm{c}} = \frac{9 \ln\left(\frac{N}{2}\right)}{2N^2}, \tag{16}$$

where N is the number of particles making up the chain. These scaling parameters arise from a balance between magnetic and viscous torques acting on a rigid chain with length approximated as $L = 2aN$. These scaling parameters ensure that the data is represented independently of the chain length and H_o. As illustrated in figures 10(a) and (b), $U^{\mathrm{b}}_{\mathrm{max}}$ showcases a nonmonotonic trend with the frequency ratio. Hence, the greatest deformation of the chains does manifest at intermediate frequencies. Interestingly, we find that the maximum $U^{\mathrm{b}}_{\mathrm{max}}$ for all experimental and numerical cases occurs at $f/f_{\mathrm{c}} \sim 0.3$.

A nonmonotonic frequency dependence is common in magnetic [36, 64–66] and elastic systems [67] at low Reynolds number driven to nonequilibrium conditions by external torques. For example, the propulsion velocity, tip trajectory, and amount of transported fluid exhibit such a trend in studies of magnetic chains serving as artificial flagella [68, 69] or cilia [70, 71], actuated by circular, oscillating, and conical magnetic fields. The nonmonotonic behavior in transport performance parameters was demonstrated to be associated to the extent of deformation of the chain undergoing periodic dynamics. In these studies, the periodic deformation appeared because one of the chain ends was attached to a large nonmagnetic particle or to a rigid surface. Consider a magnetic cilium as an example. At low frequencies, the cilium does not bend significantly during the cycle because the radial components of the magnetic forces are strong compared to drag so they maintain the cilium-like chain as a straight rod [58]. The straight chain cannot induce any net fluid flow. Conversely, at high frequencies the drag prevents the deformation that emerges from the free end to propagate deeply toward the pinned end [38, 68], decreasing the pumping performance [70, 71]. Hence, the optimum deformation to pump the surrounding fluid occurs in the intermediate frequency range. Even though the nonmonotonic trend is a common feature in these systems, the mechanism responsible for the deformation differs for each one due to the type of magnetic field employed and the constraint on the chain ends [58]. These differences are apparent when considering our analysis of the chain dynamics within a single field period and the fact that the Z-shape and 4-mode morphologies described here are novel shapes for chains in time-varying fields. Consequently, we do not expect the other systems in the literature to maximize their deformation around the frequency ratio of 0.3 that we have found for our free-end chains in the eccentric fields.

The chain morphology that tends to form at the frequency ratio of 0.3 is the Z-shape. In fact, this is the main configuration acquired by the chain within the shadowed area enclosed by $0.16 \lesssim f/f_{\mathrm{c}} \lesssim 0.6$. The other two characteristic morphologies appear outside this region of frequencies, as annotated in figure 10(a). However, there are some exceptions to this trend that must be addressed. Rigid chains in the simulations ($\mathrm{Mn} = 100$) do not deform into Z-shapes or 4-mode structures. Additionally, short chains from experiments ($N = 15$) do showcase the Z-shape but not the 4-mode conformation. In these cases, the nonmonotonic trend in $U^{\mathrm{b}}_{\mathrm{max}}$ with frequency is still observed but the morphologies are S-shapes. Such exceptions point to an unaccounted effect of the elastic forces relative to the magnetic and viscous terms in our analysis of the dynamics. We have established that in stage III the repulsive dipolar interactions overcome the flexural rigidity, so the propagating deflection grows in curvature. As shown in figure 10(a), at any given f/f_{c}, $U^{\mathrm{b}}_{\mathrm{max}}$ increases as Mn becomes larger. For a constant chain length, lower values of Mn imply either a weak H_o or a large bending rigidity (equation (14)). Therefore, for $\mathrm{Mn} = 100$, the rigidity prevents the drastic coarsening of the chain curvature, explaining why the S-shape

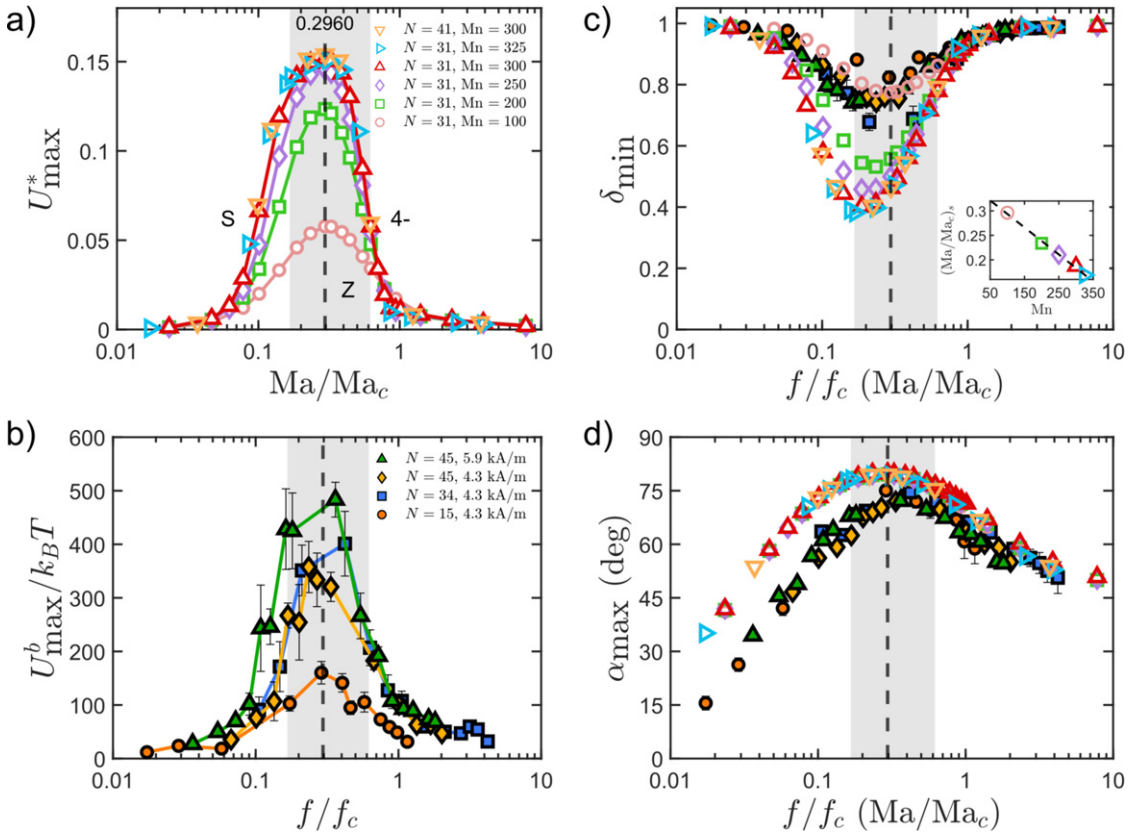

Figure 10. Nonmonotonic trends of the peak values of the deformation parameters with f (or Ma) and their scaling with the critical magnetoviscous frequency f_c or the equivalent Mason number Ma$_c$. The peak in the bending energy ($U^b_{\max}$) first increases and then decreases with frequency as seen for (a) simulations and (b) experiments. $U^b_{\max}$ is greatest at the ratio $f/f_c = \text{Ma}/\text{Ma}_c \sim 0.3$ (dashed line), independently of the chain length, H_o, or Mn. At this ratio, the chains tend to acquire Z-shape configurations. The Z-shape is also the most prevalent morphology observed in the intermediate frequency ratios of $\sim 0.16 - 0.6$, indicated by the shaded region. At lower and higher frequencies, the chains tend to acquire S-shape and 4-mode configurations, respectively. Note: $U^*_{\max} = 12U^b_{\max}/a\pi L^2\mu_o\chi^2H_o^2$. (c) Peaks in the asphericity ($\delta_{\min}$) also follow a nonmonotonic behavior. The smallest values of $\delta_{\min}$ occur at Ma/Ma$_c$ smaller than 0.3 as Mn is increased. Inset: the decrease in Mason number ratio corresponding to the smallest $\delta_{\min}$, (Ma/Ma$_c$)$_s$, is linear with Mn. (d) Collapse of $\alpha_{\max}$ with f/f_c. The largest phase lags at the intermediate frequencies (shaded region) indicate that the repulsive interactions are strongest for Z-shapes.

cannot transition into the Z-shape even for the largest $\alpha_{\max}$. Similarly, the 4-mode shape cannot form at high f/f_c because the rigidity impedes the viscous friction from deflecting the chain in stage I, despite the drag overcoming the magnetic torque.

Regardless of Mn, $U^b_{\max}$ is maximized at the same ratio of 0.3. Interestingly, the frequency ratio that minimizes $\delta_{\min}$ does not remain constant. Instead, figure 10(c) reveals that the smallest $\delta_{\min}$ shifts to lower values of Ma/Ma$_c$ as Mn is increased. Additionally, this shift decreases linearly with Mn as shown in the inset of figure 10(c). Contrary to what is expected, this trend in $\delta_{\min}$ highlights that the Z-shape with highest curvature (at $f/f_c \sim 0.3$) does not necessarily arise from the least compact intermediary S-shape.

The chains that do not form the two novel morphologies and the shift in smallest $\delta_{\min}$ to lower frequencies indicate that further analysis is required to determine the impact of the elastic properties on the chain dynamics and the conditions that lead to each of the characteristic morphologies. A state diagram probing multiple Mn and Ma would be an approach to completely identify the conditions that produce the three characteristic morphologies in the eccentric field, similar to the diagrams built for chains in conventional circular fields [30, 31] and precessing fields [58], as well as for semiflexible polymers under shear flow [4].

Considering that f_c represents the frequency at which the chain dynamics transition from synchronous rotation to asynchronous motion [29, 54, 55, 72], we would expect to observe the largest $U^b_{\max}$ at a frequency ratio closer to unity. Note, however, that the definition of f_c (equation (15)) is usually derived from a torque balance with a conventional circular field. After performing a torque balance under an eccentric field, we also find f_c as a characteristic scaling in the resulting differential equation (see appendix). Therefore, f_c proves to be a scaling parameter that is independent of the type of applied field, but its meaning changes according to the nature of the magnetic field. For our study, $f \sim 0.3f_c$ could signify the frequency necessary to maximize the repulsive interactions during stage III to bend the chains as most as possible. This idea is supported by figure 10(d), which shows the maximum global phase lag ($\alpha_{\max}$) for each f/f_c. Once again, the largest $\alpha_{\max}$ happens around $f/f_c \sim 0.3$. Furthermore, the decrease in $\alpha_{\max}$ as the frequency ratio increases beyond 0.3 also helps explain why we do not observe 4-mode structures with larger

bending energy than the Z-shapes even though more arches are formed. Simply, the repulsive interactions achieved at the corresponding frequencies are not strong enough compared to the repulsion attained for Z-shapes. Besides a slight downward shift in the experimental results of $\alpha_{\max}$ compared to the simulations, which could be attributed to chain–wall interactions, the consistent trends and the collapse of the data suggest that our interpretation of f_c in an eccentric field is appropriate.

5. Conclusions

Semiflexible colloidal chains deform periodically into different morphologies according to the frequency of an externally applied eccentric magnetic field. These morphologies are the S-shape, Z-shape, and 4-mode structure. The Z and 4-mode shapes are novel configurations in the context of chains immersed in a viscous fluid and exposed to a time-varying field. Each of these morphologies is short-lived within a cycle and displays distinct features in the geometric parameters that describe the extent of the chain's deformation. The time-varying magnitude and direction of the eccentric field ensure the periodic nature of the chain dynamics, which can be decomposed into four stages of motion. These stages are described in terms of the intricate relationship between the instantaneous field magnitude, field direction, chain orientation, bending rigidity, and the accompanying response in the geometric deformation parameters.

The mechanism for deformation observed here differs from conventional buckling under static fields. Under an eccentric field, the deformation arises from a deflection at the chain ends that propagates inward and then coarsens in curvature due to repulsive dipolar interactions that overcome the bending rigidity. For this deflection to arise and repeat periodically, stages of rotation and arrested motion are necessary to ensure that the dipolar interactions become repulsive. Additional deflection events at high frequencies, appearing at separate stages of the dynamics, lead to the onset of more arches that constitute the 4-mode structure. This behavior highlights a new pathway for the controllable folding of semiflexible paramagnetic chains. The fact that the folded morphologies restraighten consistently in the eccentric field rather than collapsing into compact states opens up new possibilities for the implementation of these nonequilibrium chains as reconfigurable devices capable of micromechanical tasks. Since the stages of the dynamics correspond to specific portions of the field period, modifications to the eccentric field could extend the duration of the deformation stage and even drive the folding of more complex morphologies that expand these potential capabilities.

The scaling analysis developed here demonstrates that by knowing a chain's critical frequency, the type of morphology and the extent of stored elastic energy can be controlled consistently in an eccentric field. Furthermore, experiments can be designed to operate at an intermediate frequency domain to maximize the bending energy via the formation of a Z-shape during stage III of the dynamics for potential applications in micro-scale transport processes. We envision these periodic dynamics to be useful for the design of freely suspending chains that act as pumps in microfluidic channels. Whether the surrounding flow field induced by the deformation and stretching events is significant to drive the transport of small materials remains an open question for future research. In spite of the remaining unknowns related to the elastic forces, our findings have provided great detail on the response of semiflexible colloidal chains under a complex time-varying magnetic field.

Acknowledgments

This work was funded by the National Science Foundation under Grant No. CBET-1705703.

Appendix.

The balance of magnetic and viscous torques on a rigid chain of length $L \sim 2aN$ is performed in this appendix to demonstrate that the critical frequency f_c remains as a characteristic scaling even when applying an eccentric time-varying field.

The expression for the magnetic torque used here is the approximation introduced in references [26, 31], which is based on the assumptions proposed by Petousis *et al* [55]. However, the difference here is that the magnitude of the field changes with time. Then, the magnetic torque is

$$\Gamma_m = \frac{1}{6}\pi a^3 N \mu_o \chi^2 ||\mathbf{H}(t)||^2 \sin(2\alpha) \tag{A.1}$$

where $||\mathbf{H}(t)||^2$ is the magnitude of equation (1). For $\lambda_x = \lambda_y = 1$, the time-varying magnitude of the field becomes

$$||\mathbf{H}(t)|| = H_o[2\sin(\omega t) + 2\cos(\omega t) + 3] = H_o\Omega(t) \tag{A.2}$$

in which $\omega = 2\pi f$.

Using the shish-kebab approximation [45], the viscous torque can be expressed as [30]

$$\Gamma_v = \frac{8\pi\eta a^3 N^3}{3\ln\left(\frac{N}{2}\right)}\frac{\mathrm{d}\theta}{\mathrm{d}t} \tag{A.3}$$

where θ is the orientation of the chain and $\mathrm{d}\theta/\mathrm{d}t$ is its angular velocity. The orientation of the chain can be expressed in terms of the field orientation ϕ and the phase lag angle α:

$$\theta(t) = \phi(t) - \alpha(t) = \tan^{-1}\left(\frac{\mathbf{H}_y(t)}{\mathbf{H}_x(t)}\right) - \alpha(t). \tag{A.4}$$

Since the driving field frequencies (and Mason numbers) used in this paper are relatively low, the torque associated to the chain's inertia can be neglected due to low Reynolds number. Hence, balancing equation (A.1) with (A.3) yields:

$$\frac{\mathrm{d}\alpha}{\mathrm{d}t} = \Phi - \frac{\mu_o \chi^2 H_o^2 \ln\left(\frac{N}{2}\right)}{16\eta N^2}[\Omega(t)]^2 \sin(2\alpha) \tag{A.5}$$

where $\Phi = -\mathrm{d}\phi/\mathrm{d}t$. The group of constants in the sinusoidal term compose the critical frequency ω_c:

$$\omega_c = \frac{\mu_o \chi^2 H_o^2 \ln\left(\frac{N}{2}\right)}{16\eta N^2}. \tag{A.6}$$

This is the same critical frequency obtained when applying a conventional circular field [26]. Therefore, f_c (equation (15)) is obtained after dividing equation (A.6) by 2π. The equivalent critical Mason number (equation (16)) is obtained after rearranging factors in equation (A.6) and considering the definition $\mathrm{Ma} = 72\eta\omega/\mu_o\chi^2 H_o^2$ [31].

ORCID iDs

Sibani Lisa Biswal https://orcid.org/0000-0002-0610-835X

References

[1] du Roure O, Lindner A, Nazockdast E N and Shelley M J 2019 Dynamics of flexible fibers in viscous flows and fluids *Annu. Rev. Fluid Mech.* **51** 539–72

[2] Munk T, Hallatschek O, Wiggins C H and Frey E 2006 Dynamics of semiflexible polymers in a flow field *Phys. Rev.* E **74** 041911

[3] Harasim M, Wunderlich B, Peleg O, Kröger M and Bausch A R 2013 Direct observation of the dynamics of semiflexible polymers in shear flow *Phys. Rev. Lett.* **110** 108302

[4] Liu Y, Chakrabarti B, Saintillan D, Lindner A and du Roure O 2018 Morphological transitions of elastic filaments in shear flow *Proc. Natl Acad. Sci. USA* **115** 9438–43

[5] Zhou Y and Schroeder C M 2016 Single polymer dynamics under large amplitude oscillatory extension *Phys. Rev. Fluids* **1** 053301

[6] Chakrabarti B, Liu Y, LaGrone J, Cortez R, Fauci L, du Roure O, Saintillan D and Lindner A 2020 Flexible filaments buckle into helicoidal shapes in strong compressional flows *Nat. Phys.* **16** 689–94

[7] Strelnikova N, Göllner M and Pfohl T 2017 Direct observation of alternating stretch–coil and coil–stretch transitions of semiflexible polymers in microstructured flow *Macromol. Chem. Phys.* **218** 1600474

[8] Vig D K and Wolgemuth C W 2012 Swimming dynamics of the Lyme disease spirochete *Phys. Rev. Lett.* **109** 218104

[9] Korta J, Clark D A, Gabel C V, Mahadevan L and Samuel A D T 2007 Mechanosensation and mechanical load modulate the locomotory gait of swimming *C. elegans J. Exp. Biol.* **210** 2383–9

[10] Schoeller S F and Keaveny E E 2018 From flagellar undulations to collective motion: predicting the dynamics of sperm suspensions *J. R. Soc. Interface* **15** 20170834

[11] Lauga E and Powers T R 2009 The hydrodynamics of swimming microorganisms *Rep. Prog. Phys.* **72** 096601

[12] Dreyfus R, Baudry J, Roper M L, Fermigier M, Stone H A and Bibette J 2005 Microscopic artificial swimmers *Nature* **437** 862–5

[13] Qian B, Powers T R and Breuer K S 2008 Shape transition and propulsive force of an elastic rod rotating in a viscous fluid *Phys. Rev. Lett.* **100** 078101

[14] Hanasoge S, Hesketh P J and Alexeev A 2018 Metachronal motion of artificial magnetic cilia *Soft Matter* **14** 3689–93

[15] McMullen A, Holmes-Cerfon M, Sciortino F, Grosberg A Y and Brujic J 2018 Freely jointed polymers made of droplets *Phys. Rev. Lett.* **121** 138002

[16] Stuij S G, Jonas H J, Gong Z, Sacanna S, Kodger T E, Bolhuis P G and Schall P 2021 Revealing viscoelastic bending relaxation dynamics of isolated semiflexible colloidal polymers *Soft Matter* **17** 8291–9

[17] Vutukuri H R, Bet B, van Roij R, Dijkstra M and Huck W T S 2017 Rational design and dynamics of self-propelled colloidal bead chains: from rotators to flagella *Sci. Rep.* **7** 16758

[18] Shafiei Aporvari M, Utkur M, Saritas E U, Volpe G and Stenhammar J 2020 Anisotropic dynamics of a self-assembled colloidal chain in an active bath *Soft Matter* **16** 5609–14

[19] Martinez-Pedrero F, Ortiz-Ambriz A, Pagonabarraga I and Tierno P 2015 Colloidal microworms propelling via a cooperative hydrodynamic conveyor belt *Phys. Rev. Lett.* **115** 138301

[20] Goubault C, Jop P, Fermigier M, Baudry J, Bertrand E and Bibette J 2003 Flexible magnetic filaments as micromechanical sensors *Phys. Rev. Lett.* **91** 260802

[21] Yang T, Marr D W M and Wu N 2018 Superparamagnetic colloidal chains prepared via Michael-addition *Colloids Surf.* A **540** 23–8

[22] Keaveny E E and Maxey M R 2008 Modeling the magnetic interactions between paramagnetic beads in magnetorheological fluids *J. Comput. Phys.* **227** 9554–71

[23] Du D, Li D, Thakur M and Biswal S L 2013 Generating an *in situ* tunable interaction potential for probing 2D colloidal phase behavior *Soft Matter* **9** 6867

[24] Li D, Banon S and Biswal S L 2010 Bending dynamics of DNA-linked colloidal particle chains *Soft Matter* **6** 4197

[25] Furst E M, Suzuki C, Fermigier M and Gast A P 1998 Permanently linked monodisperse paramagnetic chains *Langmuir* **14** 7334–6

[26] Spatafora-Salazar A, Lobmeyer D M, Cunha L H P, Joshi K and Biswal S L 2021 Hierarchical assemblies of superparamagnetic colloids in time-varying magnetic fields *Soft Matter* **17** 1120–55

[27] Cebers A 2006 Flexible magnetic filaments in a shear flow *J. Magn. Magn. Mater.* **300** 67–70

[28] Soheilian R, Abdi H, Maloney C E and Erb R M 2018 Assembling particle clusters with incoherent 3D magnetic fields *J. Colloid Interface Sci.* **513** 400–8

[29] Singh H, Laibinis P E and Hatton T A 2005 Rigid, superparamagnetic chains of permanently linked beads coated with magnetic nanoparticles. Synthesis and rotational dynamics under applied magnetic fields *Langmuir* **21** 11500–9

[30] Biswal S L and Gast A P 2004 Rotational dynamics of semiflexible paramagnetic particle chains *Phys. Rev.* E **69** 041406

[31] Kuei S, Garza B and Biswal S L 2017 From strings to coils: rotational dynamics of DNA-linked colloidal chains *Phys. Rev. Fluids* **2** 104102

[32] Cebers A 2005 Flexible magnetic filaments *Curr. Opin. Colloid Interface Sci.* **10** 167–75

[33] Yang T, Tasci T O, Neeves K B, Wu N and Marr D W M 2017 Magnetic microlassos for reversible cargo capture, transport, and release *Langmuir* **33** 5932–7

[34] Cēbers A and Kalis H 2011 Dynamics of superparamagnetic filaments with finite magnetic relaxation time *Eur. Phys. J.* E **34** 30

[35] Vázquez-Montejo P, Dempster J M and de la Cruz M O 2017 Paramagnetic filaments in a fast precessing field: planar versus helical conformations *Phys. Rev. Mater.* **1** 064402

[36] Yang T, Sprinkle B, Guo Y, Qian J, Hua D, Donev A, Marr D W M and Wu N 2020 Reconfigurable microbots folded from simple colloidal chains *Proc. Natl Acad. Sci. USA* **117** 18186–93
[37] Coq N, Bricard A, Delapierre F-D, Malaquin L, du Roure O, Fermigier M and Bartolo D 2011 Collective beating of artificial microcilia *Phys. Rev. Lett.* **107** 014501
[38] Babataheri A, Roper M, Fermigier M and Du Roure O 2011 Tethered fleximags as artificial cilia *J. Fluid Mech.* **678** 5–13
[39] Du D, Hilou E and Biswal S L 2018 Reconfigurable paramagnetic microswimmers: Brownian motion affects nonreciprocal actuation *Soft Matter* **14** 3463–70
[40] Byrom J, Han P, Savory M and Biswal S L 2014 Directing assembly of DNA-coated colloids with magnetic fields to generate rigid, semiflexible, and flexible chains *Langmuir* **30** 9045–52
[41] Zhao J, Du D and Biswal S L 2018 Nonlinear multimode buckling dynamics examined with semiflexible paramagnetic filaments *Phys. Rev.* E **98** 012602
[42] Du D, Hilou E and Biswal S L 2016 Modified Mason number for charged paramagnetic colloidal suspensions *Phys. Rev.* E **93** 062603
[43] Coughlan A C H, Torres-Díaz I, Zhang J and Bevan M A 2019 Non-equilibrium steady-state colloidal assembly dynamics *J. Chem. Phys.* **150** 204902
[44] Schroeder C, Teixeira R, Shaqfeh E and Chu S 2005 Characteristic periodic motion of polymers in shear flow *Phys. Rev. Lett.* **95** 018301
[45] Doi M and Edwards S F 1988 *The Theory of Polymer Dynamics* vol 73 (Oxford: Oxford University Press)
[46] Rotne J and Prager S 1969 Variational treatment of hydrodynamic interaction in polymers *J. Chem. Phys.* **50** 4831–7
[47] Yamakawa H 1970 Transport properties of polymer chains in dilute solution: hydrodynamic interaction *J. Chem. Phys.* **53** 436–43
[48] Sherman Z M, Ghosh D and Swan J W 2018 Field-directed self-assembly of mutually polarizable nanoparticles *Langmuir* **34** 7117–34
[49] Roper M, Dreyfus R, Baudry J, Fermigier M, Bibette J and Stone H A 2006 On the dynamics of magnetically driven elastic filaments *J. Fluid Mech.* **554** 167
[50] Huang S, Pessot G, Cremer P, Weeber R, Holm C, Nowak J, Odenbach S, Menzel A M and Auernhammer G K 2016 Buckling of paramagnetic chains in soft gels *Soft Matter* **12** 228–37
[51] Kirchenbuechler I, Guu D, Kurniawan N A, Koenderink G H and Lettinga M P 2014 Direct visualization of flow-induced conformational transitions of single actin filaments in entangled solutions *Nat. Commun.* **5** 5060
[52] Becker L E and Shelley M J 2001 Instability of elastic filaments in shear flow yields first-normal-stress differences *Phys. Rev. Lett.* **87** 198301
[53] Melle S, Fuller G G and Rubio M A 2000 Structure and dynamics of magnetorheological fluids in rotating magnetic fields *Phys. Rev.* E **61** 4111–7
[54] Abdi H, Soheilian R, Erb R M and Maloney C E 2018 Paramagnetic colloids: chaotic routes to clusters and molecules *Phys. Rev.* E **97** 032601
[55] Petousis I, Homburg E, Derks R and Dietzel A 2007 Transient behaviour of magnetic micro-bead chains rotating in a fluid by external fields *Lab Chip* **7** 1746
[56] Gao Y, Hulsen M A, Kang T G and den Toonder J M J 2012 Numerical and experimental study of a rotating magnetic particle chain in a viscous fluid *Phys. Rev.* E **86** 041503
[57] Melle S and Martin J E 2003 Chain model of a magnetorheological suspension in a rotating field *J. Chem. Phys.* **118** 9875–81
[58] Coq N, Ngo S, du Roure O, Fermigier M and Bartolo D 2010 Three-dimensional beating of magnetic microrods *Phys. Rev.* E **82** 041503
[59] Belovs M and Cēbers A 2006 Nonlinear dynamics of semiflexible magnetic filaments in an ac magnetic field *Phys. Rev.* E **73** 051503
[60] Cebers A and Erglis K 2016 Flexible magnetic filaments and their applications *Adv. Funct. Mater.* **26** 3783–95
[61] Singh K, Tipton C R, Han E and Mullin T 2013 Magneto-elastic buckling of an Euler beam *Proc. R. Soc.* A **469** 20130111
[62] Vella D, du Pontavice E, Hall C L and Goriely A 2014 The *magneto-elastica*: from self-buckling to self-assembly *Proc. R. Soc.* A **470** 20130609
[63] Gerbal F, Wang Y, Lyonnet F, Bacri J-C, Hocquet T and Devaud M 2015 A refined theory of magnetoelastic buckling matches experiments with ferromagnetic and superparamagnetic rods *Proc. Natl Acad. Sci. USA* **112** 7135–40
[64] Tierno P, Golestanian R, Pagonabarraga I and Sagués F 2008 Magnetically actuated colloidal microswimmers *J. Phys. Chem.* B **112** 16525–8
[65] Cheang U K, Meshkati F, Kim D, Kim M J and Fu H C 2014 Minimal geometric requirements for micropropulsion via magnetic rotation *Phys. Rev.* E **90** 033007
[66] Casic N, Quintero N, Alvarez-Nodarse R, Mertens F G, Jibuti L, Zimmermann W and Fischer T M 2013 Propulsion efficiency of a dynamic self-assembled helical ribbon *Phys. Rev. Lett.* **110** 168302
[67] Lagomarsino M C, Capuani F and Lowe C P 2003 A simulation study of the dynamics of a driven filament in an Aristotelian fluid *J. Theor. Biol.* **224** 215–24
[68] Roper M, Dreyfus R, Baudry J, Fermigier M, Bibette J and Stone H A 2008 Do magnetic micro-swimmers move like eukaryotic cells? *Proc. R. Soc.* A **464** 877–904
[69] Gauger E and Stark H 2006 Numerical study of a microscopic artificial swimmer *Phys. Rev.* E **74** 021907
[70] Gauger E M, Downton M T and Stark H 2009 Fluid transport at low Reynolds number with magnetically actuated artificial cilia *Eur. Phys. J.* E **28** 231–42
[71] Downton M T and Stark H 2009 Beating kinematics of magnetically actuated cilia *Europhys. Lett.* **85** 44002
[72] Vázquez-Quesada A, Franke T and Ellero M 2017 Theory and simulation of the dynamics, deformation, and breakup of a chain of superparamagnetic beads under a rotating magnetic field *Phys. Fluids* **29** 032006